

Article

Multi-Conditional Optimization of a High-Specific-Speed Axial Flow Pump Impeller Based on Machine Learning

Zhuangzhuang Sun, Fangping Tang *, Lijian Shi  and Haiyu Liu

College of Hydraulic Science and Engineering, Yangzhou University, Yangzhou 225000, China

* Correspondence: tangfp@yzu.edu.cn

Abstract: In order to widen the range of high-efficiency area of a high-specific-speed axial flow pump and to improve the operating efficiency under non-design conditions, the parameters of the axial flow pump blades were optimized. An optimization system based on computational fluid dynamics (CFD), optimized Latin hypercube sampling (OLHS), machine learning (ML), and multi-island genetic algorithm (MIGA) was established. The prediction effects of three machine learning models based on Bayesian optimization, support vector machine regression (SVR), Gaussian process regression (GPR), and fully connected neural network (FNN) on the performance of the axial flow pump were compared. The results show that the GPR model has the highest prediction accuracy for the impeller head and weighted efficiency. Compared to the original impeller, the optimized impeller is forward skewed and backward swept, and the weighted efficiency of the impeller increases by 1.31 percentage points. The efficiency of the pump section at $0.8Q_d$, $1.0Q_d$, and $1.2Q_d$ increases by about 1.1, 1.4, and 1.6 percentage points, respectively, which meets the optimization requirements. After optimization, the internal flow field of the impeller is more stable; the entropy production in the impeller reduces; the spanwise distribution of the total pressure coefficient and the axial velocity coefficient at the impeller outlet are more uniform; and the flow separation near the hub at the blade trailing edge is restrained. This research can provide a reference for the efficient operation of pumping stations and the optimal design of axial flow pumps under multiple working conditions.

Keywords: axial flow pump; multi-objective optimization; machine learning; skew and sweep



Citation: Sun, Z.; Tang, F.; Shi, L.; Liu, H. Multi-Conditional Optimization of a High-Specific-Speed Axial Flow Pump Impeller Based on Machine Learning. *Machines* **2022**, *10*, 1037. <https://doi.org/10.3390/machines10111037>

Academic Editor: Davide Astolfi

Received: 15 September 2022

Accepted: 2 November 2022

Published: 7 November 2022

Publisher's Note: MDPI stays neutral with regard to jurisdictional claims in published maps and institutional affiliations.



Copyright: © 2022 by the authors. Licensee MDPI, Basel, Switzerland. This article is an open access article distributed under the terms and conditions of the Creative Commons Attribution (CC BY) license (<https://creativecommons.org/licenses/by/4.0/>).

1. Introduction

Axial flow pumps are widely used in various fields due to their large flow and low head. In some areas along rivers and lakes, the water level difference between the inlet and outlet rivers is small, and it is more suitable for the application of low-head, high-specific-speed axial flow pump [1,2]. At present, there are few models of high-specific-speed axial flow pumps. When the pump deviates from the design flow rate, the hydraulic efficiency of the pump is relatively low, and there are obvious vortices and backflow in the impeller [3–5]. Therefore, it has become an urgent problem to optimize the geometric parameters of the impeller, improve its efficiency under non-design conditions, and widen the range of its high-efficiency area.

With the development of computer technologies, optimization design methods based on a combination of CFD and optimization algorithms have been widely used. The optimization methods for the impeller of axial flow pump are mainly divided into direct optimization and surrogate model-based optimization. Direct optimization [6–8] uses global or gradient optimization algorithms to directly optimize parameters, which requires a lot of computing resources and time for high-precision simulation operations under multi-objective problems. The surrogate model [9,10] usually builds an approximate functional relationship between the impeller parameters and the target value through machine learning, which can often improve the optimization efficiency. Ma et al. [11] used a combination of radial basis function (RBF) neural network and genetic algorithm to carry out a

three-objective optimization of a double-blade sewage pump, and the RBF model predicted the results with high accuracy. Zhu et al. [12] also used this method to optimize the blade profile of a current energy turbine, which improved the hydrofoil lift–drag ratio at three angles of attack and suppressed the hydrofoil stall phenomenon. Wang et al. [13–15] used the method of coupling a response surface model, a multi-objective genetic algorithm, and an inverse problem design to carry out a multi-objective optimization of a mixed-flow pump impeller, which improved the hydraulic efficiency of the pump under multiple working conditions. Pei et al. [16] used an artificial neural network (ANN) and a particle swarm algorithm to optimize 11 shape parameters of the water inlet pipe of a vertical pipeline pump. The results showed that the ANN could accurately reflect the relationship between pump efficiency and design variables, and the maximum pump efficiency significantly improved after optimization. Miao et al. [17] optimized a hydraulic turbine blade profile based on a neural network–genetic algorithm, and improved the hydraulic efficiency of the hydraulic turbine under multiple operating conditions. In addition, Feng [18], Zhang [19], Wang [20–22] et al. adopted the method of combining machine learning and optimization algorithm to optimize hydraulic machinery.

In the field of hydraulic machinery, machine learning is also widely used in performance prediction and state recognition. He et al. [23] predicted the gas–liquid two-phase pressure rise of a centrifugal pump based on machine learning, and the prediction result had a true value error of less than 15%. Yang et al. [24] used the proper orthogonal decomposition and SVR model to achieve rapid prediction of the temperature distribution and the overflow water distribution on the outer surface of a hot gas anti-icing skin. Wang et al. [25] established a performance prediction model for semi-hermetic reciprocating compressors based on the BP network. Huang et al. [26] proposed a centrifugal pump energy performance prediction model based on a hybrid neural network. Compared to the experimental value, the mean square error (MSE) value was less than 0.02. Li et al. [27] proposed a new method to measure the gas–liquid flow rate of wet gas by combining a conical throttling device with machine learning techniques, and predicted the gas-phase and liquid-phase flow rates in the throttling device. Chen et al. [28] determined the identification of different leakage states of hydraulic pumps based on the wavelet decomposition and deep neural network, and the identification accuracy reached 99.3%. Panda et al. [29] used a support vector machine method to diagnose and classify centrifugal pump faults at different speeds, and showed high accuracy in multiple fault classifications. Bordoloi et al. [30] used a support vector machine (SVM) model for the diagnosis of clogging levels and cavitation degrees at different pump speeds. Rapur et al. [31] also used SVM to monitor the status of the blockage of the inlet pipe of a centrifugal pump under different flow rates and rotational speeds.

The geometric parameters of the impeller of an axial flow pump mainly include the solidity, the stagger angle of the hydrofoil, and the maximum camber of the hydrofoil. In addition to the above parameters, the stacking modes of the hydrofoils also have a great influence on the performance of the impeller. The stacking modes are divided into circumferential “skew” (the stacking point moves circumferentially) and axial “sweep” (the stacking point moves axially). It is usually defined that the stack point movement is “forward” when it is in the same direction of rotation or in the opposite direction to the mainstream, and “backward” when it is in the opposite direction of rotation or in the same direction as the mainstream [32,33]. Appropriate skew and sweep can realize the redistribution of the flow and load in the spanwise direction and reduce the loss of secondary flow. At present, the skew and sweep are often ignored or optimized separately during the impeller optimization of axial flow pumps, and the impeller parameters are not optimized as a whole [34,35]. Based on the above research findings, three different machine learning models are used in this paper to construct the approximate functional relationship between the impeller solidity, the stagger angle, the skew and sweep parameters, and the target value. At the same time, the prediction results of the machine learning models are evaluated, and the optimal model is selected as the proxy model. Finally, the MIGA

is selected as the optimization algorithm to optimize multi-conditions, which provides a reference for the design of axial flow pumps in multi-conditions.

2. Research Object

Taking a large-scale, low-head pumping station as the object, the pumping station has a design head of 3.15 m, a single-machine flow rate of $64 \text{ m}^3/\text{s}$, an impeller diameter of 4.4 m, a pump speed of 85.7 r/min, and a specific speed of about 1060. It is a typical low-head pumping station. After being converted to a model pump with an impeller diameter of 300 mm according to the principle of equal nD values, the model pump design has a flow rate $Q_d = 297.51 \text{ L/S}$ and a speed $n = 1256.93 \text{ r/min}$, and the design head of the pump has $H_d = 3.32 \text{ m}$. According to the research and analysis of pump station selection, the hydraulic model is ZM25. The main design parameters of the ZM25 model are as follows: the number of blades is 3, the hub ratio is 0.35, the number of guide vanes is 5, and the solidity at the hub and the shroud of the impeller blade is 0.754 and 0.58, respectively. A three-dimensional model of the pump section is shown in Figure 1.

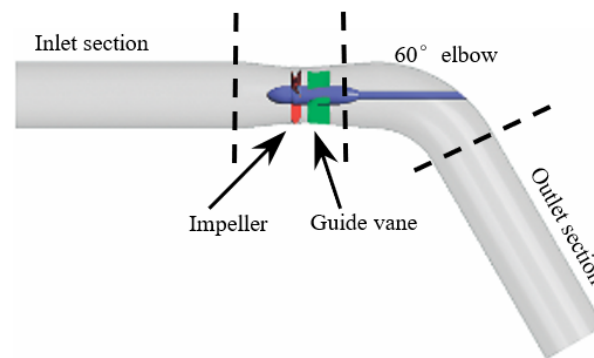


Figure 1. Three-dimensional model of the pump section.

3. Numerical Calculation Method

3.1. Turbulence Model and Boundary Conditions

The steady performance of an axial flow pump attracts more attention during the optimal design of the axial flow pump, so steady numerical calculation is adopted. The Reynolds-averaged N-S equations are solved using ANSYS CFX, and the equations are closed with the SST $k-\omega$ model [36,37]. The discrete format of the advection scheme and turbulence numerics is “High Resolution”. The inlet adopts the mass flow inlet condition, and the outlet adopts the pressure outlet condition. The entire computational domain is divided into a rotating domain and a static domain, in which the impeller is a rotating domain and the rest are static domains. The “Stage” model (also known as the Mixing-Plane model) is used to deal with the parameter transfer of the flow in the dynamic and static couplings between the inlet and outlet of the impeller. The no-slip condition is applied to the solid wall, while the automatic wall treatment in CFX is used in the near-wall region to accommodate the turbulent flow model.

3.2. Meshing and Irrelevance Analysis

The hexahedral structured mesh is divided using the block strategy, and the mesh near the wall is refined. The y^+ of the main flow components, such as the impeller, is all within 100, which basically meets the requirements of the application of the SST $k-\omega$ turbulence model for the quality of near-wall mesh [38]. Among them, the inlet section, the outlet section, and the elbow section are meshed using ICEM, and the O-block topology is adopted. The impeller and guide vane section are meshed using TurboGrid and the J/O topology and H/O topology, respectively, while periodically arranging the flow channels. For areas with complex structures, appropriate mesh refinement is done. The tip gap size is 0.2 mm, and 15 nodes are arranged in the gap. We keep the same topology structure, modify the maximum mesh size to generate different numbers of meshes, and use the

calculation result of the head under the design flow as the index to perform mesh irrelevance analysis. The results are shown in Figure 2. When the number of full machine grids increases to 4.11 million, continuing to increase the grid has little effect on the calculation results. Considering the calculation accuracy and calculation time, the number of grids is determined to be 4.11 million. The final grid is shown in Figure 3.

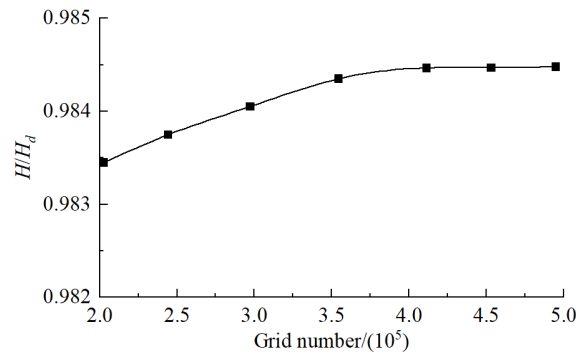


Figure 2. Grid independency test.

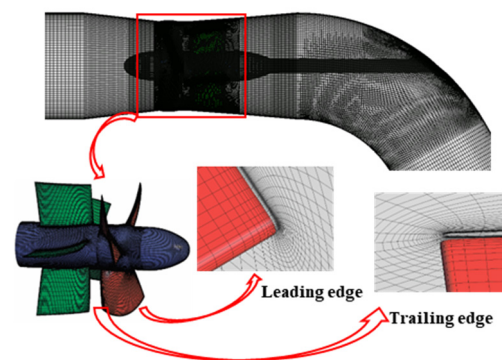


Figure 3. Meshing of Pump Sections.

3.3. Verification of Numerical Calculation Results

Figure 4 is a comparison diagram of the CFD results of the external characteristics of the pump section and the experimental (EXP) results. The numerical simulation results are basically consistent with the experimental results under different flow rates, and the head and efficiency errors near the design point are less than 3%, indicating that the numerical calculation method is reasonable and the results have high accuracy.

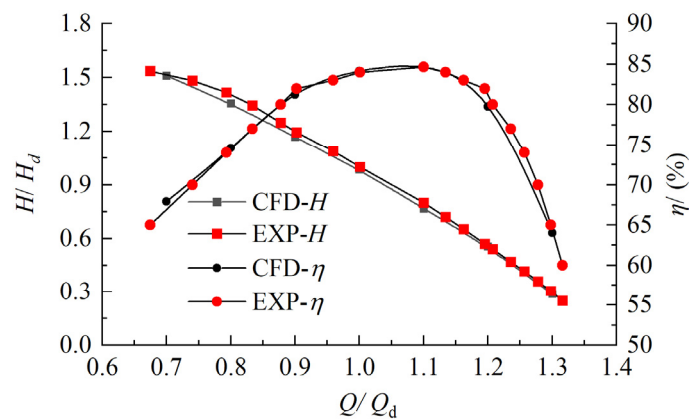


Figure 4. Comparison of the CFD results and the experiment results on hydraulic performance.

4. Machine Learning Models

4.1. Support Vector Machine Regression

Support vector machine regression (SVR) is a general machine learning method proposed by the statistician Vapnik [39,40]. Using the idea of support vector, it can non-linearly map low-dimensional data to a high-dimensional space, so that linear regression can be solved in the high-dimensional space. The prediction function has the following form:

$$\hat{Y} = \kappa^T \varphi(X) + b \quad (1)$$

where X is the input variable; \hat{Y} is the predicted value of the variable; Y is the real value of the variable; $\varphi(X)$ is the nonlinear function that maps the sample to the high-dimensional space; and κ and b are the undetermined parameters, which are also the keys to the training of the SVR model.

SVR aims to find a hyperplane in a multi-dimensional space, so that all the data in a set are closest to the plane. Specifically, given the accuracy ε ($\varepsilon \geq 0$), the error between the predicted value and the actual value is not greater than ε ; that is, the prediction can be considered correct, no loss is calculated, and only the loss of data points with an error greater than ε is calculated. Introducing the slack variables ζ and ζ^* ($\zeta, \zeta^* \geq 0$) and regularization parameter C ($C > 0$), κ and b training is transformed into an optimization problem:

$$\begin{aligned} \min & \left(\frac{1}{2} \kappa^T \kappa + C \sum_{i=1}^N \zeta_i + C \sum_{i=1}^N \zeta_i^* \right) \\ \text{s.t.} & \omega^T \varphi(X_i) + b - Y_i \leq \varepsilon + \zeta_i^* \\ & -\omega^T \varphi(X_i) - b + Y_i \leq \varepsilon + \zeta_i \end{aligned} \quad (2)$$

where X_i is the i -th input variable.

This optimization problem can be transformed into a Lagrangian dual form, whereby the prediction function is equal to the following equation:

$$\hat{Y}(x) = \sum_{i=1}^N (\alpha_i - \alpha_i^*) K(X, X_i) + b \quad (3)$$

where α_i^* and α_i are the Lagrangian multipliers, and $K(X, X_i) = \varphi(X) \varphi^T(X_i)$ is the kernel function.

4.2. Gaussian Process Regression

A common application of Gaussian process (GP) in machine learning is the Gaussian process regression (GPR) [39,41], which has good applicability to dealing with complex problems, such as small samples, nonlinearity, and high dimensionality. The derivation of the Gaussian process regression can also start from a general linear regression, and a general linear regression model with noise has the following form:

$$\hat{Y} = X^T \kappa + \theta \quad (4)$$

where θ follows a Gaussian distribution with mean 0 and standard deviation σ , $\theta \sim N(0, \sigma^2)$, where any Gaussian distribution is completely determined by its first and second central moments (mean function and covariance function). The GPR introduces the functions $f(X)$ ($f(X)$ follows a Gaussian distribution with mean 0 and covariance function $k(X, X_i)$) and $h(X)$ (basis functions) to interpret this response and to project the functions to a high-dimensional space.

$$\hat{Y} = h(X)^T \kappa + f(X) \quad (5)$$

The GPR model is a probabilistic model, and each observation x_i introduces a latent variable $f(X_i)$, making the GPR model nonparametric.

4.3. Fully Connected Neural Network

A complete fully connected neural network (FNN) [39,42] consists of an input, a fully connected layer, an activation function, and an output. The first fully connected layer of the neural network connects the input layer, and the fully connected layer consists of a weight matrix and a bias vector. Each fully connected layer multiplies the input by a weight matrix and then adds a bias vector. The activation function is the function that operates on the neurons of the neural network and is responsible for mapping the input of the neuron to the output. In machine learning, parameters, such as the weight matrices of the fully connected layers, are updated after each iteration. When the model encounters noisy samples, the parameters of the fully connected layer will also be synchronized with the noise (the weight matrix changes greatly), resulting in overfitting. Therefore, a regularization method is introduced into the model. The L_2 regularization method is a common regularization method to reduce overfitting, and a penalty coefficient is added to the weight matrix to avoid overfitting caused by too large parameters in the weight matrix.

4.4. Data Standardization and Evaluation Indicators

The data need to be preprocessed before training to improve the training effect. The Z-score standardization method is used to make the data conform to the Gaussian distribution with mean 0 and variance 1. The formula is as follows:

$$X^* = \frac{X - \mu}{\sigma^2} \quad (6)$$

where μ is the mean value.

In order to evaluate the prediction performance of the model, the correlation coefficient R^2 , the mean square error (MSE), the mean absolute percentage error (MAPE), the relative absolute error (RAE), and the Willmott's Index of Agreement (WIA) are introduced as evaluation indicators, and the relevant definitions are as follows:

$$R^2 = 1 - \frac{\sum_{i=1}^N (Y_i - \hat{Y}_i)^2}{\sum_{i=1}^n (Y_i - \bar{Y})^2} \quad (7)$$

$$\text{MSE} = \frac{1}{N} \sum_{i=1}^N (Y_i - \hat{Y}_i)^2 \quad (8)$$

$$\text{MAPE} = \frac{100}{N} \sum_{i=1}^N \frac{|Y_i - \hat{Y}_i|}{Y_i} \quad (9)$$

$$\text{RAE} = \frac{\sum_{i=1}^N |Y_i - \hat{Y}_i|}{\sum_{i=1}^n |Y_i - \bar{Y}|} \quad (10)$$

$$\text{WIA} = 1 - \frac{\sum_{i=1}^N (Y_i - \hat{Y}_i)^2}{\sum_{i=1}^N (|Y_i - \bar{Y}| + |\hat{Y}_i - \bar{Y}|)^2} \quad (11)$$

Among the evaluation indicators, the smaller the RMSE, MAPE, and RAE are, and the closer R^2 and WIA are to 1, the more accurate the prediction results are.

4.5. Hyperparameter Optimization

Hyperparameters are parameters that cannot be obtained through learning in machine learning models (such as the kernel functions of SVR and GPR models, and the number

of fully connected layers of FNN models), and their selection directly affects the training effect of the model. Hyperparameter optimization in machine learning aims to find the hyperparameter combination that makes the machine learning algorithm perform the best on the validation set. Manual parameter tuning requires a lot of experience and is time-consuming. Therefore, many automatic parameter tuning methods have been developed, such as grid search, random search, and Bayesian optimization. In grid search and random search, each hyperparameter is independent of each other, and the previous calculation result does not affect the latter calculation result, which usually takes more time. Bayesian optimization uses Bayes' theorem to estimate the posterior distribution of the objective function based on the data, and then selects the next sampled hyperparameter combination based on the distribution. It makes full use of the information of the previous sampling point, and its optimization works by learning the shape of the objective function and finding the parameters that can improve the result to the global maximum. Therefore, this paper adopts the Bayesian optimization method when adjusting the hyperparameters. In order to prevent overfitting during model training, a 5-fold cross-validation is used, and the principle of minimum mean square error (MSE) is used for 100 iterations. Table 1 shows the hyperparameters and the search range of the hyperparameters in each ML model.

Table 1. Hyperparameter and its search range in each ML model.

Model	Hyperparameter and Its Search Range
SVR	Kernel functions: Gaussian, linear, cubic, and quadratic Regularization factor: [0.001,1000] Kernel scale: [0.001,1000] ϵ : [0.001,100]/1.349·iqr(Y)
GPR	Basis functions: zero, constant, and linear. Kernel functions: Non-isotropic and isotropic exponential, quadratic rational, squared exponential, Matern 5/2, and Matern 3/2 Kernel scale: [0.001, 1] · (max(X)–min(X)) Standard Deviation: [0.0001, max (0.001, 10×std(Y))]
FNN	Number of fully connected layers: [1,2,3] Size of each connection layer: [1,300] Activation function: Rectified Linear Unit (RELU), Tanh, None, and Sigmoid Regularization strength: [0,1250]

5. Optimization Method of Impeller

5.1. Optimization Objective

According to the needs of working on multiple operating conditions, the weighted efficiency η_d under the conditions of $0.8Q_d$, $1.0Q_d$, and $1.2Q_d$ is taken as the optimization target. In the optimization process, a large number of sample points need to be obtained, and the full flow channel calculation requires a lot of computing resources and time, so only single-channel calculation is used for the impeller. At the same time, the head change should not be too large under the design flow to ensure that the specific revolutions are consistent, so that the axial flow pump can meet the design requirements in engineering applications. The head change before and after the impeller optimization is restricted to be less than 0.1 m. The optimization model is defined as follows:

$$\begin{aligned} \eta_d &= k_1\eta_1 + k_2\eta_2 + k_3\eta_3 \\ \text{s.t. } H_{ip2} &= H_{ip1} \pm 0.1 \end{aligned} \quad (12)$$

where η_1 , η_2 , and η_3 are the impeller efficiencies under the conditions of $0.8Q_d$, $1.0Q_d$, and $1.2Q_d$, respectively; k_1 , k_2 , and k_3 are the weighting factors and, based on the relevant literature [6], the values are 0.2786, 0.4059, and 0.315, respectively; H_{ip} is the impeller head under the design flow; and H_{ip1} and H_{ip2} are the impeller head under the design flow before and after optimization, in m.

5.2. Optimization Parameters

There are 11 sections from the hub to the shroud, and the section hydrofoil is NACA66 (mod). The spanwise dimensionless distance r^* is defined as follows:

$$r^* = \frac{r - r_h}{r_t - r_h} \quad (13)$$

where r is the radius of the section; r_t is the radius at the shroud of the blade; and r_h is the radius at the hub of the blade, in m.

The main design parameters of the blade include the following: the solidity c/t (where c is the chord length and t is the pitch, in m), the stagger angle β , and the maximum camber ratio a/c , as shown in Figure 5. By specifying the hydrofoil stagger angles β_1 , β_2 , and β_3 , and maximum camber ratios $(a/c)_1$, $(a/c)_2$, and $(a/c)_3$ of section $r^* = 0, 0.47$ and 1 , the remaining section parameters can be obtained using quadratic function interpolation. Given the solidity $(c/t)_1$ and $(c/t)_2$ at the hub and the shroud of the blade, the chord lengths of the remaining sections are obtained using linear interpolation.

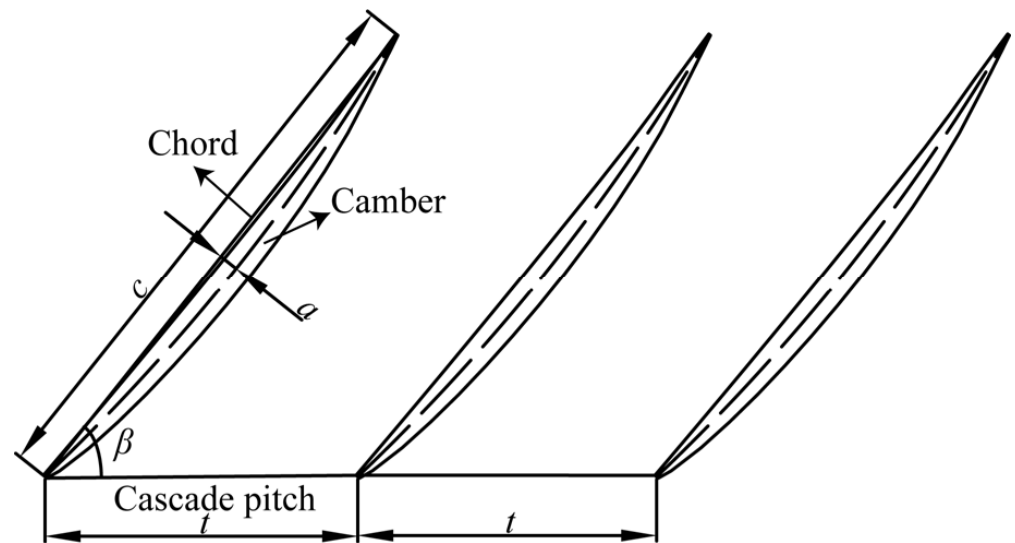


Figure 5. Schematic diagram of the blade parameters.

Taking the circumferential angle and the axial displacement at the hub as 0, the circumferential skew angles α_1 and α_2 and the axial sweep displacements γ_1 and γ_2 of the $r^* = 0.47$ and 1 sections are specified. The skew and sweep parameters of the remaining sections are also obtained using quadratic function interpolation. Among them, the circumferential skew angle and the axial sweep displacement are “+”, which means backward skew and backward sweep, respectively. The schematic diagram of the blade stacking modes is shown in Figure 6.

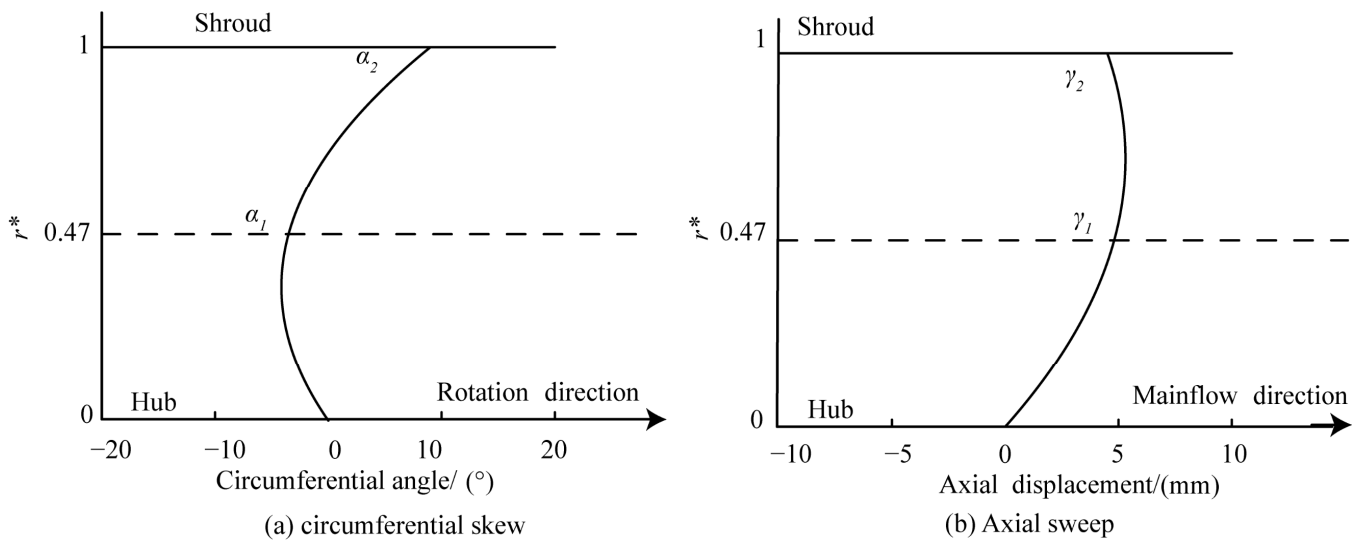


Figure 6. Schematic diagram of the blade stacking modes.

Based on the above analysis, the impeller has a total of 12 design parameters, and the value range of each parameter is shown in Table 2. Among them, the variation range of the solidity, hydrofoil stagger angle, and hydrofoil camber is $\pm 10\%$ of the original values.

Table 2. Range of design parameters.

Design Parameters	Low Level (–)	High Level (+)
$(c/t)_1/-$	0.679	0.829
$(c/t)_2/-$	0.522	0.638
$\beta_1/^\circ$	39.435	48.199
$\beta_2/^\circ$	24.816	30.330
$\beta_3/^\circ$	15.817	19.331
$(a/c)_1/\%$	5.470	6.686
$(a/c)_2/\%$	3.154	3.854
$(a/c)_3/\%$	1.362	1.664
γ_1/mm	–5	10
γ_2/mm	–5	10
$\alpha_1/^\circ$	–15	15
$\alpha_2/^\circ$	–15	15

5.3. Optimization Progress

The optimization process is shown in Figure 7. First, an optimized Latin hypercube sampling (OLHS) is used to obtain sample data within the design range. An automatic numerical simulation platform is built through I sight to quickly obtain the optimal target value of the sample point, and the approximate relationship between the variables and the optimization target is fitted through machine learning. After comparing the training results of the SVR, GPR, and FNN models, the appropriate approximate model is selected. Finally, the approximate model is solved using the multi-island genetic algorithm (MIGA) to obtain the optimal parameter combination, which will be confirmed by CFD. The MIGA is essentially an improvement of the parallel distributed genetic algorithm, which has better global solving ability and computing efficiency than traditional genetic algorithms [43]. Therefore, the MIGA is selected for global optimization.

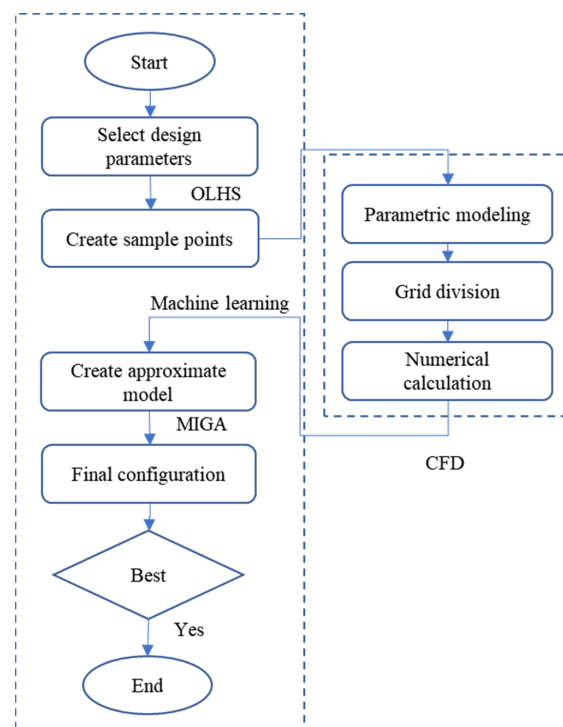


Figure 7. Optimization progress.

6. Results & Analysis

6.1. Data Set Partitioning

In the optimization process, the predicted variables are the weighted efficiency η_d and the impeller head H_{ip2} . The OHLS is used to generate 516 sets of samples, of which 85% are used for training and 15% are used for testing. Table 3 shows the results of the division of the sample set. The statistical characteristics of the training set and the test set are similar and highly representative.

Table 3. Data set partitioning.

Data Set		Sample Size	Max Value	Min Value	Mean Value	Standard Deviation
H_{ip2}	Training set	439	5.123	1.952	3.494	0.660
	Testing set	77	5.114	1.993	3.540	0.669
η_d	Training set	439	91.796	73.497	88.707	2.281
	Testing set	77	91.972	79.107	88.795	1.904

6.2. Comparison of Training Results

The hyperparameters after Bayesian optimization are used to establish the prediction model. Table 4 shows the comparison of the indicators of the prediction results of the three machine learning models. It can be seen from the table that the GPR model has the highest prediction accuracy for H_{ip2} and η_d , and the model has high generalization ability. On the training set of H_{ip2} , the evaluation indicators R^2 , MSE, MAPE, RAE, and WIA of the GPR model are 0.997, 0.001, 0.772, 0.047, and 0.999, respectively. On the testing set of H_{ip2} , the evaluation indexes R^2 , MSE, MAPE, RAE, and WIA of the GPR model are 0.998, 0.001, 0.634, 0.041, and 1.000, respectively. On the training set of η_d , the evaluation indicators R^2 , MSE, MAPE, RAE, and WIA of the GPR model are 0.988, 0.063, 0.198, 0.101, and 0.997, respectively. On the test set of η_d , the evaluation indicators R^2 , MSE, MAPE, RAE, and WIA of the GPR model are 0.981, 0.070, 0.195, 0.124, and 0.995, respectively.

Table 4. Comparison of the prediction results of the three models.

Evaluation Indicators	SVR		GPR		FNN		
	Training Set	Testing Set	Training Set	Testing Set	Training Set	Testing Set	
H_{ip2}	R^2	0.995	0.997	0.997	0.998	0.982	0.991
	MSE	0.002	0.001	0.001	0.001	0.008	0.004
	MAPE	1.016	0.945	0.772	0.634	2.082	1.416
	RAE	0.061	0.058	0.047	0.041	0.122	0.087
	WIA	0.999	0.999	0.999	1.000	0.995	0.998
η_d	R^2	0.937	0.898	0.988	0.986	0.971	0.954
	MSE	0.324	0.364	0.063	0.070	0.150	0.166
	MAPE	0.440	0.429	0.198	0.195	0.346	0.348
	RAE	0.224	0.270	0.101	0.124	0.179	0.222
	WIA	0.984	0.975	0.997	0.995	0.993	0.988

Figure 8 shows the probability distribution functions (PDF) of the predicted and observed H_{ip2} and η_d . From the shape of the PDF, there is a certain gap between the predicted values of the SVR, GPR, and FNN models and the observed values when the η_d is less than 80% in the prediction of efficiency. When the η_d is greater than 80%, the GPR model shows the best agreement with the observations, followed by the FNN and SVR models. In the prediction of H_{ip2} , all three models produce acceptable predictions. However, the GPR model shows the best agreement with the observed values, with the GPR model in the box plots predicting results that are closer to the median, the upper

quartile, and the lower quartile. In addition, the Taylor diagram of the prediction results of the SVR, GPR, and FNN models for H_{ip2} and η_d is shown in Figure 9. For the prediction of H_{ip2} and η_d , the GPR model is closer to the position of the target point, and its prediction results are the most accurate.

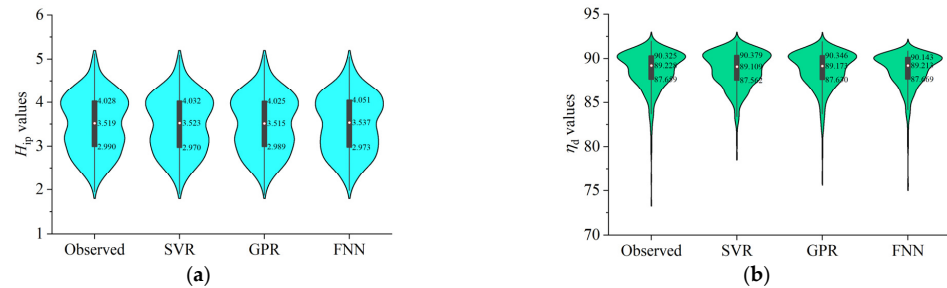


Figure 8. PDF of predicted and observed values: (a) H_{ip2} and (b) η_d .

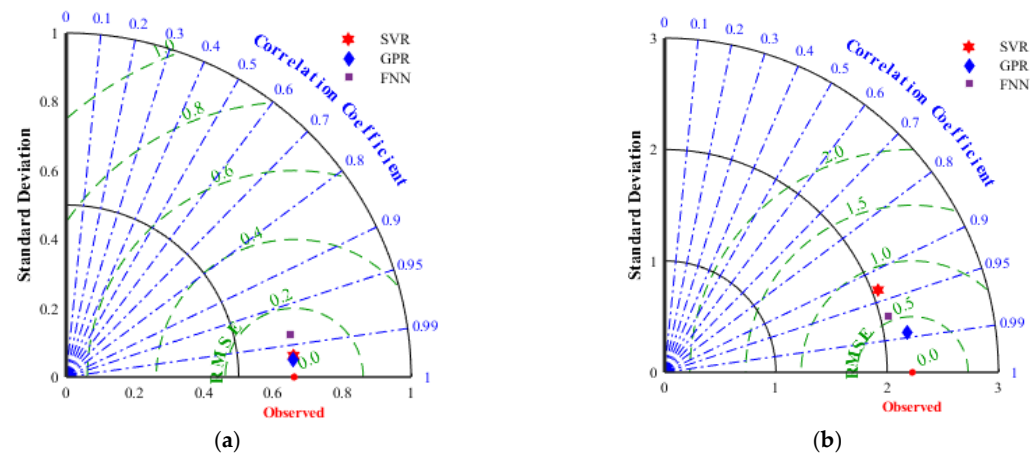


Figure 9. The Taylor diagram of predicted and observed values: (a) H_{ip2} and (b) η_d .

Figure 10 shows the relative deviation (RD) of all models on the training and test data. The smaller the RD range of the model is, the more efficient the model results are. For the prediction results of H_{ip2} , the RD of the GPR model is in the range of $[-4, 4]$ and $[-2, 2]$ in the training and testing sets. Compared to the SVR model (training set $[-4, 6]$ and testing set $[-4, 4]$) and the FNN model (training set $[-15, 15]$ and testing set $[-7, 10]$), the margin of error is smaller. For the prediction results of η_d , the RD of the GPR model is mainly distributed in the range of $[-1, 1]$ on the training and testing sets. The range is smaller compared to the SVR ($[-2, 2]$) and FNN ($[-1.5, 1]$) models. When combining the cumulative frequency and the absolute relative deviation (ARD) percentages (see Figure 11), for the prediction results of H_{ip2} , the cumulative frequency of the GPR model is within 3% and the ARD is 98.64%, which is significantly higher than that of the SVR (96.71%) and FNN (78.87%) models. For the prediction of η_d , the cumulative frequency of the GPR model is within 1% and the ARD is 99.41%, which is also higher than that of the SVR (92.64%) and FNN (97.09%) models. Based on the above analyses, it can be seen that the GPR model has a higher prediction accuracy for the weighted efficiency and the impeller head, and the GPR model is finally determined as the proxy model for impeller optimization.

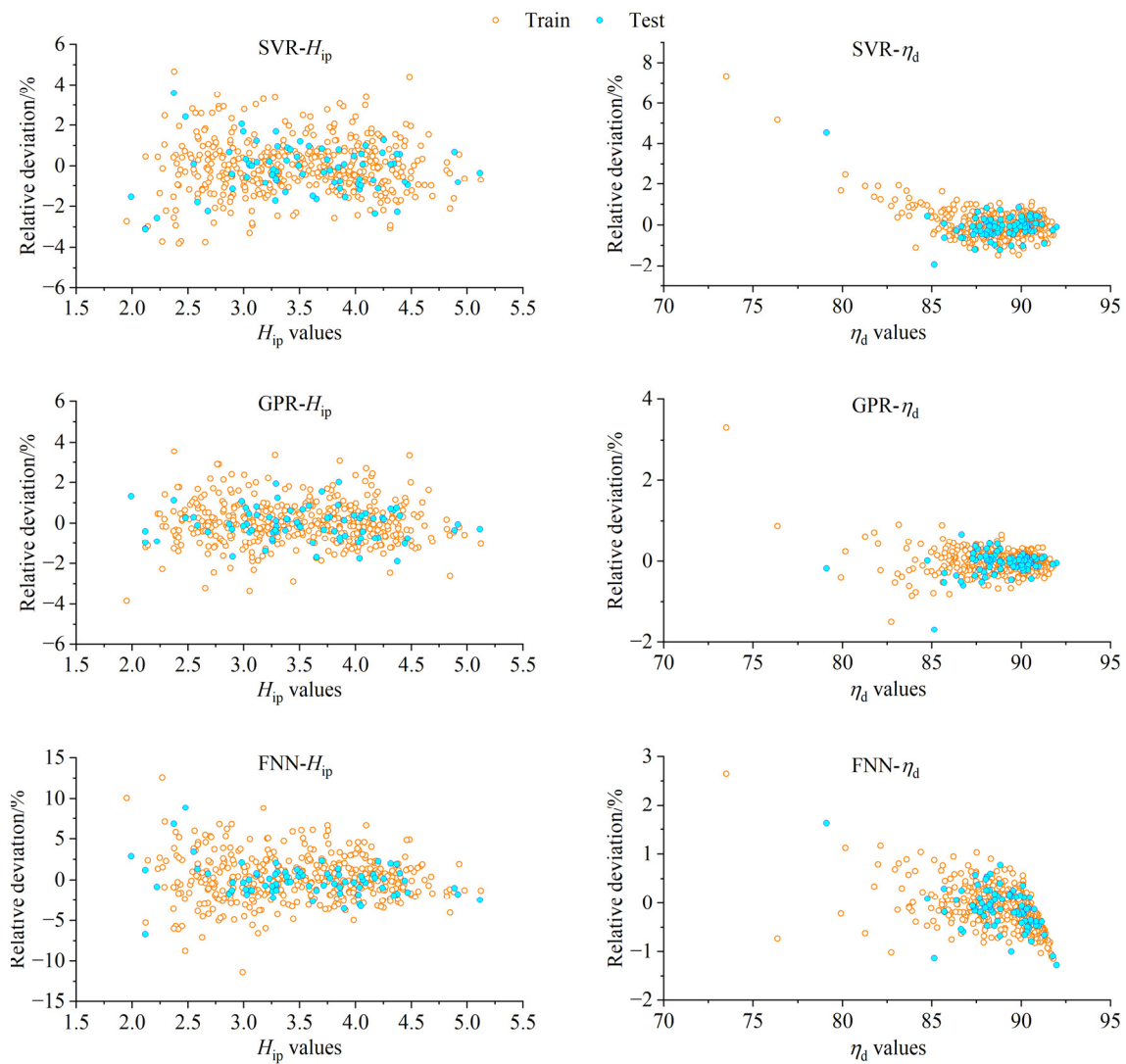


Figure 10. The relative deviation in H_{ip2} and η_d of the three models.

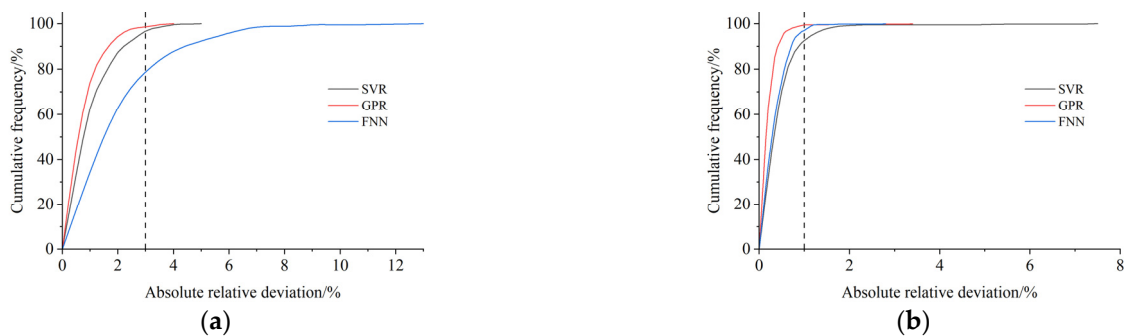


Figure 11. The cumulative frequency of absolute relative deviation: (a) H_{ip2} and (b) η_d .

6.3. Analysis of Optimization Results

The prediction model obtained through the GPR training is further optimized based on the multi-island genetic algorithm. The algorithm is set as follows: the number of subgroups is 20, the number of islands is 20, the crossover rate is one, the inter-island mobility and the mutation probability are both 0.01, and the migration interval is five generations [43]. According to the optimization results of the MIGA, the CFD calculation is re-calculated, and the main parameters of the optimized impeller are obtained (see

Table 5). The optimized parameters are within the allowable range. After optimization, the axial direction of the blade is backward and the circumferential direction is skewed forward. The shape of the impeller is shown in Figure 12. The hydrofoil stagger angle at the blade hub increases, while the hydrofoil stagger angle at the blade shroud decreases, indicating that the work at the blade hub increases and the work at the blade tip decreases, which balances the outlet head of the blade. The solidity at the hub and the shroud of the blade increases, and the chord length of the blade becomes longer as a whole. At the same time, the reduction of the maximum camber of the hydrofoil is also conducive to the improvement of the lift–drag ratio of the hydrofoil at a small angle of attack, which means the blade has a higher hydraulic efficiency at a large flow. The weighted efficiency and the head of the optimized impeller are 92.22% and 3.699 m, respectively, which is 1.31 percentage points higher than the original impeller’s weighted efficiency. The change of the impeller head under the design flow is less than 0.04 m, which meets the optimization requirements. At the same time, the weighted efficiency and the impeller head predicted by the GPR model are 92.18% and 3.704 m, respectively, which are 0.04 percentage points and 0.005 m away from the actual values of the numerical simulation. This proves the high precision of the GPR model.

Table 5. Comparison of the parameters between the original and optimized models.

Design Parameters	Original	Optimized
$(c/t)_1/-$	0.754	0.819
$(c/t)_2/-$	0.580	0.594
$\beta_1/^\circ$	43.817	47.792
$\beta_2/^\circ$	27.573	28.106
$\beta_3/^\circ$	17.574	16.847
$(a/c)_1/\%$	6.078	5.571
$(a/c)_2/\%$	3.503	3.845
$(a/c)_3/\%$	1.513	1.655
γ_1/mm	0	6.531
γ_2/mm	0	6.981
$\alpha_1/^\circ$	0	−3.93
$\alpha_2/^\circ$	0	−7.98
$\eta_d/\%$	90.91	92.22
H_{ip}/m	3.660	3.699

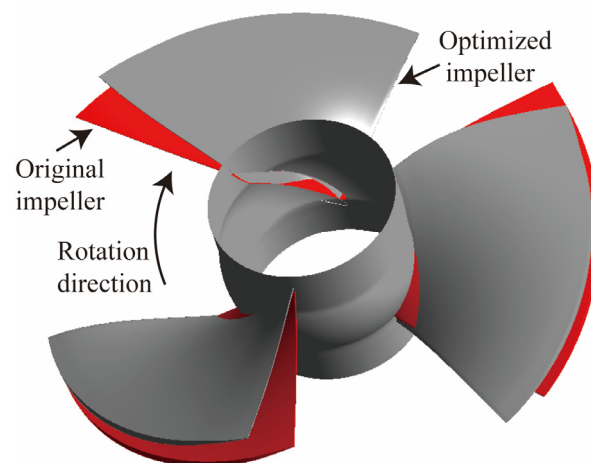


Figure 12. Comparison of the impeller shapes before and after optimization.

In order to further analyze the performance changes of the optimized axial flow pump under multiple working conditions, the optimized impeller plus the flow-passing components, such as guide vanes, are combined to form the axial flow pump section for

numerical calculation. When comparing the performance curves obtained using CFD of the pump section before and after optimization (see Figure 13), the efficiency curve of the pump section after optimization is overall higher than the original design curve. Under the flow conditions of $0.8Q_d$, $1.0Q_d$, and $1.2Q_d$, the efficiencies are 75.71%, 85.53%, and 81.38%, and the efficiency increases by about 1.1, 1.4, and 1.6 percentage points, respectively. After optimization, the high-efficiency area of the axial flow pump is significantly wider.

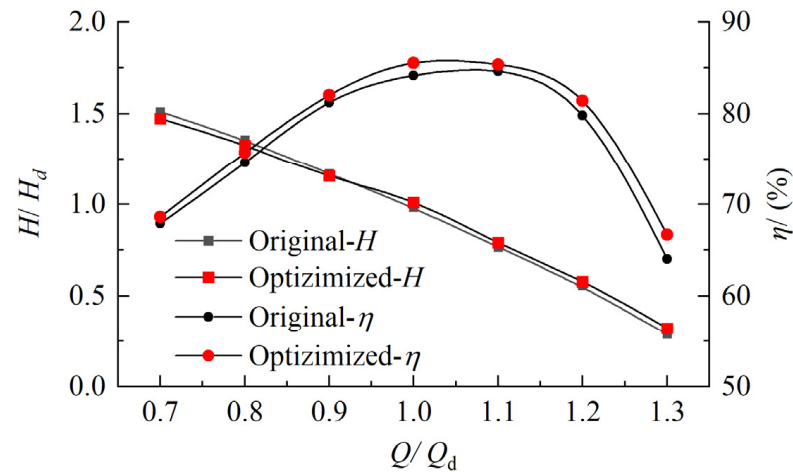


Figure 13. Performance comparison of the pump section before and after optimization.

6.4. Analysis of the Internal Flow Field of the Impeller before and after Optimization

To better compare the variation in the flow field parameters, the following dimensionless parameters are defined.

Velocity coefficient:

$$v^* = \frac{v}{u_t} \quad (14)$$

Total pressure rise coefficient:

$$P_t^* = \frac{P_t - P_{tin}}{0.5\rho u_t^2} \quad (15)$$

Static pressure coefficient:

$$P^* = \frac{P - P_{in}}{0.5\rho u_t^2} \quad (16)$$

where v is velocity; u_t is the circumferential velocity at the shroud, in m/s; P_t and P are the total pressure and static pressure, in Pa; P_{tin} and P_{in} are the inlet total pressure and static pressure, in Pa; and ρ is the density, in kg/m^3 .

When comparing the axial velocity coefficient v_t^* distribution of the impeller outlet before and after optimization (see Figure 14a), it can be seen that, under different flow conditions, the axial velocity distribution at the blade outlet after optimization shows a trend of decreasing at the blade shroud and increasing at the blade hub, and the axial velocity distribution in the entire spanwise direction is more uniform. At the same time, under the condition of $0.8Q_d$, the axial velocity near the blade hub is negative, indicating that there is a small-scale recirculation zone there, which results in energy loss, and the scope of the recirculation zone is significantly reduced after optimization. The change of the total pressure rise coefficient P_t^* (see Figure 14b) at the impeller outlet is similar to the change of the axial velocity. The total pressure rise coefficient increases at the blade hub and decreases at the blade shroud. The total pressure rise coefficient of the original model has a negative value near the hub under the flow condition of $0.8Q_d$, which means that the impeller in this area does negative work. After optimization, this phenomenon is

eliminated and the distribution of the total pressure at the impeller outlet is more uniform, indicating that the flow state at the impeller outlet has significantly improved.

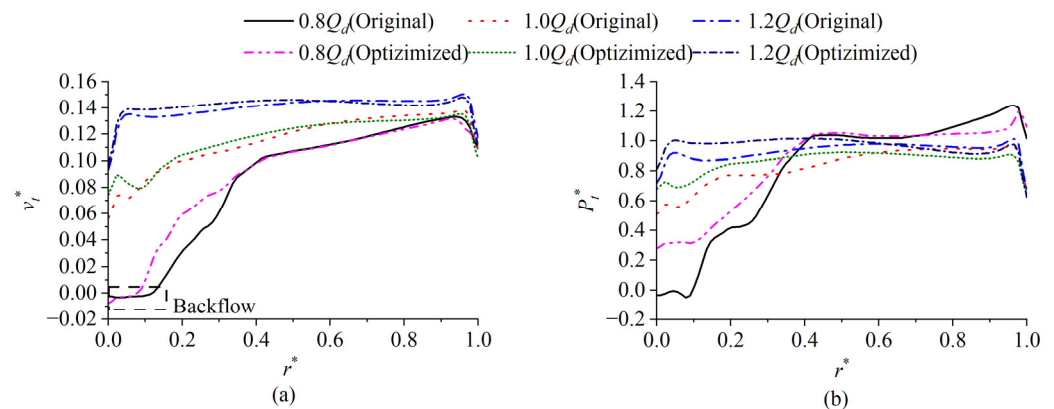


Figure 14. Comparison of the flow field at the impeller outlet: (a) axial velocity coefficient v_t^* , and (b) total pressure rise coefficient P_t^* .

Figure 15 shows the static pressure coefficient and the streamline distribution on the blade surface. As can be seen from Figure 15a, due to the influence of the hub (the hub is spherical), a small range of flow separation is formed near the outlet side of the pressure surface of the blade under the conditions of $1.0Q_d$ and $1.2Q_d$. Under the condition of $0.8Q_d$, the flow separation area of the pressure surface of the original model accounts for about 1/5 of the blade area. This is mainly due to the strong backflow intensity at the hub and the secondary flow formed by the interaction between the backflow and the mainstream, which causes the streamline near the hub at the outlet side to flow from the hub to the middle of the blade. At the same time, an obvious saddle point and a node are formed on the pressure surface of the blade, which results in obvious flow separation. After optimization, the backflow intensity weakens and the flow separation area significantly reduces. As can be seen from Figure 15b, a flow separation phenomenon near the outlet side hub of the suction surface of the blade is observed. It can be seen from the pressure distribution on the surface of the blade that the pressure distortion phenomenon occurs in the hub at the outlet of the suction surface of the blade, resulting in the pressure gradient direction being perpendicular to the mainstream direction, which increases the pressure difference between the shroud and the hub on the blade surface and leads to the secondary flow from the hub to the shroud. After optimization, the flow separation area under each flow condition significantly reduces; the pressure distribution on the surface of the blade is more reasonable; and the pressure distortion near the outlet side hub becomes suppressed.

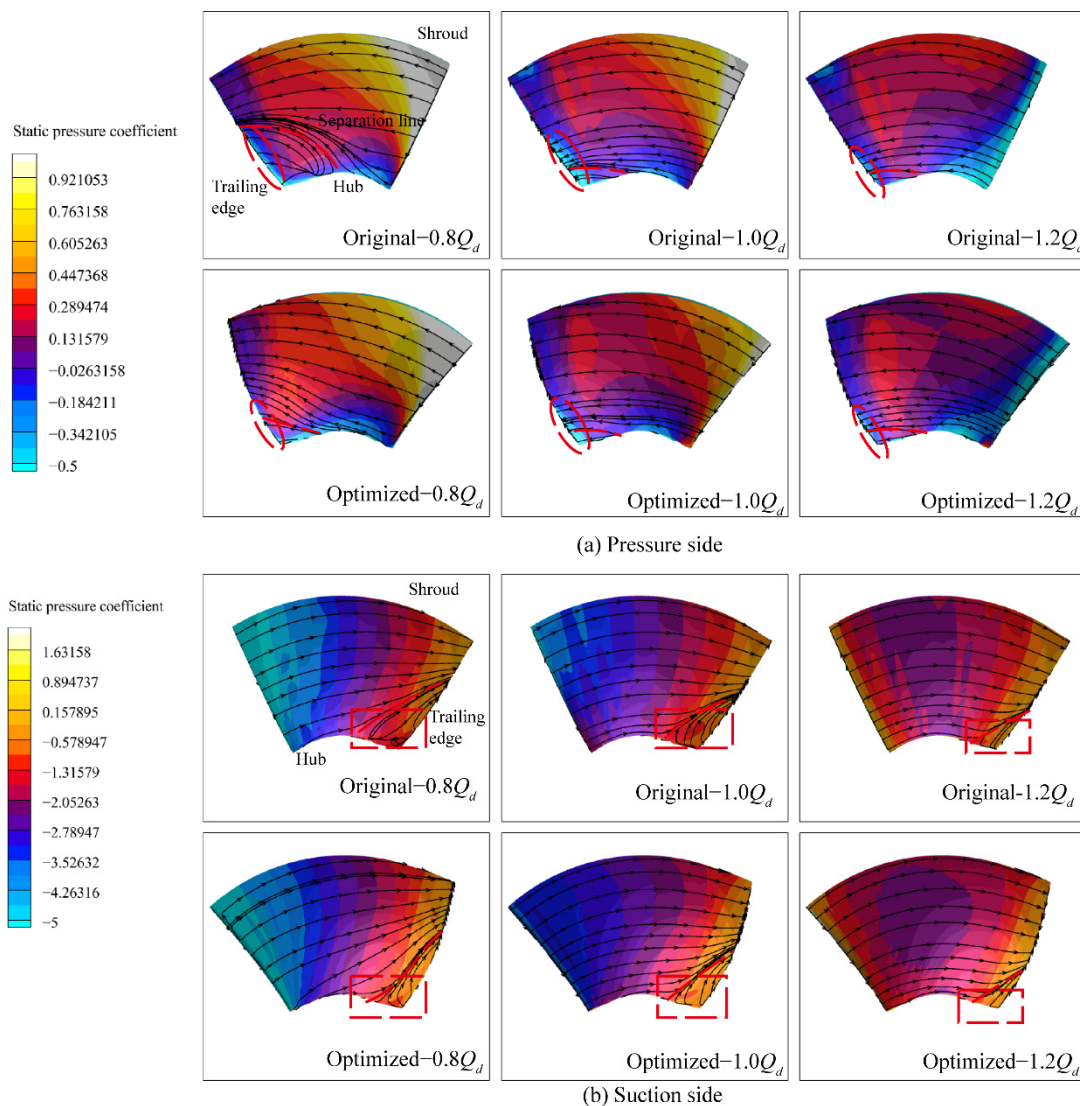


Figure 15. Surface pressure and streamline distribution of the blade.

When the fluid works inside the pump, due to the action of viscous force and internal friction, a part of the energy is converted into the internal energy of the system, and the entropy increases during the whole process. In recent years, the entropy production theory has been widely used in the analysis of the internal flow loss of hydraulic machinery [44,45]. Compared to the traditional differential pressure method, the entropy production theory can directly reflect the position of energy loss, which has guiding significance for the optimal design of hydraulic machinery. For turbulent flow, the entropy generation rate can be divided into two parts: one is caused by the average velocity, called the direct dissipation term, and the other is caused by the pulsating velocity, called the turbulent dissipation term. The entropy production rate (EPR) is defined as follows:

$$\dot{S}_D''' = \dot{S}_D''' + \dot{S}_D''' \tag{17}$$

where \dot{S}_D''' is the EPR; \dot{S}_D''' is the EPR caused by the average speed; and $\dot{S}_{D'}'''$ is the EPR caused by the pulsating speed, in $\text{W m}^{-3}\text{K}^{-1}$. The entropy production caused by the average speed is defined as follows:

$$\begin{aligned} \dot{S}_D''' &= \frac{\mu}{T} \left[\left(\frac{\partial \bar{u}}{\partial y} + \frac{\partial \bar{v}}{\partial x} \right)^2 + \left(\frac{\partial \bar{u}}{\partial z} + \frac{\partial \bar{w}}{\partial x} \right)^2 + \left(\frac{\partial \bar{v}}{\partial z} + \frac{\partial \bar{w}}{\partial y} \right)^2 \right] \\ &+ 2 \frac{\mu}{T} \left[\left(\frac{\partial \bar{u}}{\partial x} \right)^2 + \left(\frac{\partial \bar{v}}{\partial y} \right)^2 + \left(\frac{\partial \bar{w}}{\partial z} \right)^2 \right] \end{aligned} \quad (18)$$

where \bar{u} , \bar{v} , and \bar{w} are the components of the velocity in the x , y , and z directions, in m/s ; μ is the dynamic viscosity, in $\text{Pa}\cdot\text{s}$; and T is the temperature, in K .

The pulsation entropy production can be approximated using the following formula:

$$\dot{S}_{D'}''' = \psi \cdot \frac{\rho f k}{T} \quad (19)$$

where the coefficient ψ is 0.09; f is the turbulence eddy frequency, in s^{-1} ; and k is the turbulent kinetic energy, in m^2/s^2 . Figure 16 shows the comparison of the internal entropy production rate of the impeller before and after optimization under different flow conditions. Under the condition of $1.2Q_d$, the entropy production in the impeller is mainly concentrated on the blade surface and near the wake vortex. However, under the flow conditions of $0.8Q_d$ and $1.0Q_d$, there is a large area of high entropy production near the exit of the $r^* = 0.02, 0.5$ section, which is related to the backflow and the flow separation analyzed above. Compared to the original model, under the condition of $0.8Q_d$, the entropy production on the blade surface slightly increases, but the backflow and the flow separation near the outlet are restrained, and the entropy production near the impeller outlet significantly reduces. The entropy production on the blade surface decreases under $1.0Q_d$ and $1.2Q_d$, and the entropy production area near the outlet also decreases significantly under $1.0Q_d$.

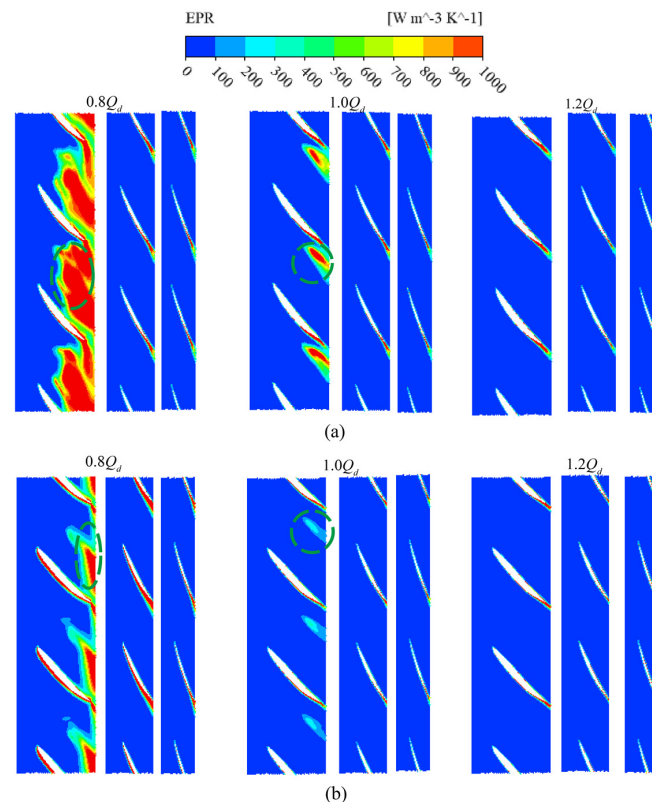


Figure 16. The distribution of EPR in the impeller:(a) Original impeller, and (b) Optimized impeller. (From left to right of each item is $r^* = 0.02, 0.5$, and 0.98).

7. Conclusions

In order to improve the hydraulic efficiency of a high-specific-speed axial flow pump impeller under multiple working conditions, the parameters of the blade, such as the solidity, the hydrofoil stagger angle, and the skew and sweep, are optimized. The specific conclusions are as follows:

1. An optimization system composed of the CFD, OLHS, ML, and MIGA is proposed, which provides a reference for the optimal design of axial flow pumps in the future.
2. Based on Bayesian optimization, the hyperparameters of the SVR, FNN, and GPR models are optimized, and the optimized hyperparameter combination is used to establish the prediction model of the weighted efficiency and the impeller head. Compared to the SVR and FNN models, the GPR model has better generalization and the highest prediction accuracy, and the GPR model is better adaptable to the nonlinear relationship between the fit optimization parameters and the target in the optimal design.
3. Compared to the original model, the weighted efficiency of the optimized impeller increases by 1.31 percentage points, and the efficiency of the pump section at $0.8Q_d$, $1.0Q_d$, and $1.2Q_d$ increases by about 1.1, 1.4, and 1.6 percentage points, respectively. The operating range of the high-efficiency area of the axial flow pump is improved.
4. The optimized impeller is forward skewed and backward swept, which is beneficial for reducing flow separation on the blade surface. After optimization, the flow field at the impeller outlet significantly improves; the total pressure and the axial velocity along the spanwise direction are more uniform; the flow separation at the trailing edge of the blade improves; and the entropy production in the impeller reduces.

Author Contributions: Data curation, Z.S.; Formal analysis, F.T.; Writing—original draft, Z.S.; Writing—review & editing, L.S.; Software, H.L. All authors have read and agreed to the published version of the manuscript.

Funding: This research work was supported by the National Natural Science Foundation of China (Grant No. 51376155), the National Natural Science Foundation of China (Grant No. 52209116), the Jiangsu Province Water Conservancy Science and Technology Project (Grant No. 2021012), and the Yangzhou Science and Technology Plan Project City-School Cooperation Special Project (Grant No. YZ2022178).

Institutional Review Board Statement: Not applicable.

Informed Consent Statement: Not applicable.

Data Availability Statement: The data presented in this study are available on request from the corresponding author.

Acknowledgments: This is a project funded by the Priority Academic Program Development (PAPD) of the Jiangsu Higher Education Institutions Support for construction.

Conflicts of Interest: The authors declare no conflict of interest.

References

1. Liu, C. Researches and Developments of Axial-flow Pump System. *Trans. Chin. Soc. Agric. Mach.* **2015**, *46*, 11.
2. Wang, Z.; Peng, G.; Zhou, L.; Hu, D. Hydraulic performance of a large slanted axial-flow pump. *Eng. Comput.* **2010**, *27*, 243–256. [[CrossRef](#)]
3. Yang, J.; Guan, X. Hydraulic Design of High Specific Speed Model Axial-flow Pump. *Trans. Chin. Soc. Agric. Mach.* **2008**, *39*, 4.
4. Shi, W. Design of Axial Flow Pump Hydraulic Model ZM931 On High Specific Speed. *Trans. Chin. Soc. Agric. Mach.* **1998**, *29*, 49–53.
5. Tang, F.; Wang, G.; Liu, C.; Zhou, J.; Cheng, L. Design and Numerical Analysis On An Axial-flow Pump With High Specific Speed. *J. Mech. Eng.* **2005**, *41*, 5. [[CrossRef](#)]
6. Yuan, J.; Fan, M. Orthogonal optimum design method for high specific-speed axial-flow pumps. *Trans. Chin. Soc. Agric. Eng.* **2018**, *37*, 22.
7. Tao, R.; Xiao, R.; Yang, W. Optimization design for axial flow pump based on genetic algorithm. *J. Drain. Irrig. Mach. Eng.* **2018**, *36*, 7.

8. Wang, L.; Wang, T.; Luo, Y. Improved NSGA- in Multi-Objective Optimization Studies of Wind Turbine Blades. *Appl. Math. Mech.* **2011**, *32*, 739–748. [[CrossRef](#)]
9. Mu, X.; Yao, W.; Yu, X.; Liu, K.; Xue, F. A survey of surrogate models used in MDO. *Chin. J. Comput. Mech.* **2005**, *22*, 5.
10. Gu, H.; Lin, Y.; Hu, Z.; Yu, J. Surrogate Models Based Optimization Methods for the Design of Underwater Glider Wing. *J. Mech. Eng.* **2009**, *45*, 8. [[CrossRef](#)]
11. Ma, S.B.; Kim, S.; Kim, J.H. Optimization design of a two-vane pump for wastewater treatment using machine-learning-based surrogate modeling. *Processes* **2020**, *8*, 1170. [[CrossRef](#)]
12. Zhu, G.; Feng, J.; Guo, P.; Luo, X. Optimization of hydrofoil for marine current turbine based on radial basis function neural network and genetic algorithm. *Trans. Chin. Soc. Agric. Eng.* **2014**, *30*, 9.
13. Wang, M.; Li, Y.; Yuan, J.; Yuan, S. Effects of different vortex designs on optimization results of mixed-flow pump. *Eng. Appl. Comput. Fluid Mech.* **2022**, *16*, 36–57. [[CrossRef](#)]
14. Wang, M.; Li, Y.; Yuan, J.; Meng, F.; Chen, J. Comprehensive Improvement of Mixed-Flow Pump Impeller Based on Multi-Objective Optimization. *Processes* **2020**, *8*, 905. [[CrossRef](#)]
15. Wang, M.; Li, Y.; Yuan, J.; Yuan, J.; Osman, F.K. Matching Optimization of a Mixed Flow Pump Impeller and Diffuser Based on the Inverse Design Method. *Processes* **2021**, *3*, 260. [[CrossRef](#)]
16. Pei, J.; Gan, X.; Wang, W.; Yuan, S.; Tang, Y. Hydraulic Optimization on Inlet Pipe of Vertical Inline Pump Based on Artificial Neural Network. *Trans. Chin. Soc. Agric. Mach.* **2018**, *49*, 8.
17. Miao, S.; Yang, J.; Wang, X.; Li, J.; Li, T. Blade pattern optimization of the hydraulic turbine based on neural network and genetic algorithm. *J. Aerosp. Power* **2015**, *30*, 8.
18. Feng, Y. Multi-Objective Optimum Design of Centrifugal Double-channel Pump Based on RBF Neural Network and Particle Swarm Optimization Algorithm. Ph.D. Thesis, Jiangsu University, Zhenjiang, China, 2018.
19. Zhang, X.; Hu, B.; Feng, Y.; Liu, K.; Wang, C. Multi-objective optimization design of screw centrifugal pump based on RBF neural network and differential evolution algorithm. *J. Drain. Irrig. Mach. Eng.* **2022**, *40*, 7.
20. Wang, C.; Ye, J.; Zeng, C.; Xia, Y.; Luo, B. Multi-objective optimum design of high specific speed mixed-flow pump based on NSGA-genetic algorithm. *Trans. Chin. Soc. Agric. Eng.* **2015**, *31*, 7.
21. Wang, C.; Feng, Y.; Ye, J.; Luo, B.; Liu, K. Multi-objective parameters optimization of centrifugal slurry pump based on RBF neural network and NSGA- genetic algorithm. *Trans. Chin. Soc. Agric. Eng.* **2017**, *33*, 109–115.
22. Wang, C.; Hu, B.; Feng, Y.; Liu, K. Multi-objective optimization of double vane pump based on radial basis neural network and particle swarm. *Trans. Chin. Soc. Agric. Eng.* **2019**, *35*, 25–32.
23. He, D.; Li, R.; Sun, S.; Guo, P. Prediction of gas-liquid two-phase pressure increment of a centrifugal pump based on machine learning. *Trans. Chin. Soc. Agric. Eng.* **2022**, *38*, 9.
24. Yang, Q.; Guo, X.; Li, Q.; Dong, W. Hot air anti-icing performance estimation method based on POD and surrogate model. *Acta Aeronautica et Astronautica Sinica* **2022**, *44*, 126992.
25. Wang, W.; Yao, Y.; Ma, Z. Model of Compressor Performance Prediction Based on Error Back-propagation Artificial Neural work. *Fluid Mach.* **2005**, *33*, 4.
26. Huang, R.; Zhang, Z.; Zhang, W.; Mou, J.; Zhou, P.; Wang, Y. Energy performance prediction of the centrifugal pumps by using a hybrid neural network. *Energy* **2020**, *213*, 119005. [[CrossRef](#)]
27. Li, S.; Zhao, F.; Zheng, X.; He, D.; Bai, B. Wet gas metering by cone throttle device with machine learning. *Measurement* **2020**, *164*, 108080. [[CrossRef](#)]
28. Chen, J.; Chen, L.; Wang, Z. The Recognition of Hydraulic Pump Leakage State Based on Wavelet Decomposition and Deep Learning. *Modul. Mach. Tool Autom. Manuf. Tech.* **2021**, *4*, 006.
29. Panda, A.; Rapur, J.; Tiwari, R. Prediction of flow blockages and impending cavitation in centrifugal pumps using Support Vector Machine (SVM) algorithms based on vibration measurements. *Measurement* **2018**, *130*, 44–56. [[CrossRef](#)]
30. Bordoloi, D.J.; Tiwari, R. Identification of suction flow blockages and casing cavitations in centrifugal pumps by optimal support vector machine techniques. *J. Braz. Soc. Mech. Sci. Eng.* **2017**, *39*, 2957–2968. [[CrossRef](#)]
31. Rapur, S.; Tiwari, R. Severity Assessment and Classification of Blockage of Centrifugal Pumps in Frequency Domain of Vibration Data Using Support Vector Machine Algorithms. In Proceedings of the Vibrations in Rotating Machinery (VIRM-11), Manchester, UK, 13–15 September 2016.
32. Zhang, S.; Tian, S.; Zhang, X.; Li, H.; Xi, D.; He, W.; Zhang, A. Research Progress of Skew and Sweep Aerodynamic Technology for Turbomachinery Blades. *J. Propuls. Technol.* **2021**, *42*, 15.
33. Mao, M.; Song, Y.; Wang, Z. Research on Design of Swept and Bowed Rotor in a Transonic Axial Flow Compressor. *J. Power Eng.* **2008**, *28*, 6.
34. Wei, B.; Wu, K. Review on the Research of high performance Skew-Swept Blades and Its Influence on Inner Flow. *Fluid Mach.* **2001**, *29*, 31–34.
35. Li, Y.; Ouyang, H.; Du, Z. Optimized Design Based on Skewed and Swept Blade Technology. *J. Eng. Therm. Energy Power* **2007**, *22*, 605–609.
36. Menter, F.; Kuntz, M.; Langtry, R. Ten years of industrial experience with the SST turbulence model. *Heat Mass Transf.* **2003**, *4*, 625–632.

37. Florianr, M. Zonal two equation kw turbulence models for aerodynamic flows. In Proceedings of the 23rd Fluid Dynamics, Plasmadynamics and Lasers Conference, Orlando, FL, USA, 6–9 July 1993; p. 2906.
38. Lee, K.S.; Ziaul, H.; Han, S.E. A study on the y^+ effects on turbulence model of unstructured grid for CFD analysis of wind turbine. *J. Korean Assoc. Spat. Struct.* **2015**, *15*, 75–84. [[CrossRef](#)]
39. Zhou, Z.H. *Machine Learning*; Springer Nature: Berlin/Heidelberg, Germany, 2021.
40. Vapnik, V.; Golowich, S.; Smola, A. Support Vector Method for Function Approximation, Regression Estimation and Signal Processing. *Adv. Neural Inf. Process. Syst.* **1996**, *9*, 281–287.
41. Rasmussen, C.E.; Williams, C.K.I. *Gaussian Processes for Machine Learning*; The MIT Press: Cambridge, MA, USA, 2006.
42. Hsu, K.Y.; Li, H.Y.; Psaltis, D. Holographic implementation of a fully connected neural network. *Proc. IEEE* **1990**, *78*, 1637–1645. [[CrossRef](#)]
43. Gourisaria, M.K.; Mishra, B.; Dehuri, S. A Hybrid Parallel Multi-Objective Genetic Algorithm: HybJaclScone Model. *Int. J. Comput. Appl.* **2013**, *66*, 1–6.
44. Sun, L.; Pan, Q.; Zhang, D.; Zhao, R.; van Esch, B. Numerical study of the energy loss in the bulb tubular pump system focusing on the off-design conditions based on combined energy analysis methods. *Energy* **2022**, *258*, 124794. [[CrossRef](#)]
45. Ji, L.; Li, W.; Shi, W.; Chang, H.; Yang, Z. Energy characteristics of mixed-flow pump under different tip clearances based on entropy production analysis. *Energy* **2020**, *199*, 117447. [[CrossRef](#)]